

Taylor & Francis
Taylor & Francis Group

Vehicle System Dynamics
International Journal of Vehicle Mechanics and Mobility

ISSN: 0042-3114 (Print) 1744-5159 (Online) Journal homepage: www.tandfonline.com/journals/nvsd20

Suspension parameter optimisation and staged yaw damper configuration adapted to wheel-rail contact geometry evolution

Hu Li , Yuan Yao, Zhiyong Shi & Enrico Meli

To cite this article: Hu Li , Yuan Yao, Zhiyong Shi & Enrico Meli (03 Sep 2026): Suspension parameter optimisation and staged yaw damper configuration adapted to wheel-rail contact geometry evolution, Vehicle System Dynamics, DOI: 10.1080/00423114.2026.2728165

To link to this article: https://doi.org/10.1080/00423114.2026.2728165

Published online: 03 Sep 2026.

Submit your article to this journal

View related articles

View Crossmark data

Full Terms & Conditions of access and use can be found at
https://www.tandfonline.com/action/journalInformation?journalCode=nvsd20

VEHICLE SYSTEM DYNAMICS
https://doi.org/10.1080/00423114.2026.2728165

Check for updates

Suspension parameter optimisation and staged yaw damper configuration adapted to wheel-rail contact geometry evolution

Hu Li[a,b], Yuan Yao [a], Zhiyong Shi[b] and Enrico Meli[b]

[a]State Key Laboratory of Rail Transit Vehicle System, Southwest Jiaotong University, Chengdu, People's Republic of China; [b]Department of Industrial Engineering, University of Florence, Firenze, Italy

ABSTRACT

Wheel profile evolution due to tread wear shifts the suspension parameters required for favourable vehicle dynamic performance. Conventional fixed-parameter designs often compromise across diverse contact conditions, making it difficult to maintain robust performance throughout the wheel life cycle. This paper proposes a supervisory staged configuration method for yaw dampers based on wheel-rail contact geometry. The approach implements discrete updates to yaw-damper configurations, driven by equivalent conicity, via manual adjustments during maintenance intervals. First, a linear high-speed locomotive model identifies key suspension parameters affecting hunting stability. Subsequently, a simulation-based surrogate model, integrating measured wheel profiles with SIMPACK multi-body dynamics, is constructed to optimise the matching between suspension parameters and staged yaw-damper configurations. Furthermore, an equivalent conicity observation model is developed to estimate contact states and support a geometry-dependent switching law. Finally, a 200,000 km joint wear-dynamics simulation validates the proposed method. The recommended Opt2 scheme effectively reduces wheelset lateral forces while improving hunting stability, ride quality, and wear-related indices over the wheel life cycle.

ARTICLE HISTORY
Received 5 May 2026
Revised 7 July 2026
Accepted 29 July 2026

KEYWORDS
Vehicle dynamic; yaw damper; equivalent conicity; staged configuration; wear-dynamics simulation

1. Introduction

The design of locomotive suspension parameters is closely coupled with wheel-rail contact geometry [1]. When dynamic performance is taken as the optimisation objective, different wheel-rail contact geometric conditions correspond to specific optimal suspension parameter sets. However, during the long-term service of high-speed locomotives, tread wear inevitably alters the wheel-rail contact profile, which may disrupt suspension-geometry matching. This mismatch may intensify vehicle vibration and wheel-rail dynamic interaction. Equivalent conicity is a key indicator of contact-geometry evolution. Abnormal deviations in equivalent conicity can significantly impair vehicle dynamic performance and degrade hunting stability. For high equivalent conicity caused by hollow-worn wheels,

CONTACT Yuan Yao yyuan8848@163.com

© 2026 Informa UK Limited, trading as Taylor & Francis Group

Wang and Gong reviewed the corresponding stability degradation mechanisms and countermeasures [2], while Qi et al. further investigated the characteristics of hollow wear and its suppression measures for high-speed trains [3]. Higher equivalent conicity usually occurs in the later stage of wheel wear and is prone to inducing high-frequency secondary hunting instability in the bogie. For low equivalent conicity conditions, Chang et al. analysed the mechanism of high-speed train carbody shaking caused by wheel-rail contact geometry degradation [4], and Sun et al. reported carbody hunting of an electric locomotive induced by low wheel-rail contact conicity [5]. Lower equivalent conicity is more commonly observed after thin-flange reprofiling and tends to trigger low-frequency primary hunting instability of the carbody. Since conventional fixed suspension parameters can only achieve a performance compromise among multiple operating conditions, they are often unable to satisfy the continuously evolving dynamic requirements over the entire life cycle. Consequently, state-dependent yaw damper configuration adapted to wheel-rail contact geometry evolution is required.

Extensive research has been conducted on the deterioration of locomotive dynamic performance caused by the evolution of wheel-rail contact geometry. Several studies have focused on refining wheel-rail wear simulation models and revealing the coupling mechanisms between wheel wear evolution and vehicle dynamic responses. Bosso et al. reviewed numerical models for wheel and rail profile wear simulation and summarised the general framework of wear prediction based on vehicle dynamics and contact calculation [6]. Xie et al. proposed a wheel profile wear prediction framework for high-speed trains considering tread modification [7]. Nencioni et al. developed an efficient conformal contact model for multibody and railway applications [8], while Apezetxea et al. experimentally validated a fast wheel wear prediction model [9]. H-Nia et al. further evaluated rail maintenance strategies from a life-cycle cost perspective based on simulation results [10]. With the development of data-driven techniques, Liu et al. proposed a two-step wheel tread wear prediction method based on GA-BPNN and LSTM algorithms [11], Wang et al. applied neural networks to tread wear prediction and optimisation [12], and Chen et al. developed a knowledge-informed wheel wear prediction method using multisource signal data [13]. Liu and Bruni analysed the influence of individual measured wheel profiles on the numerical assessment of rail vehicle running dynamics [14]. Gao et al. proposed a wheel wear indicator related to wheel-rail contact parameters and vehicle hunting stability [15]. Li et al. investigated the mechanisms of wheel wear evolution and wheel-rail contact geometry variation in locomotives, showing that equivalent conicity evolution can be strongly affected by the lateral migration of the nominal wear peak rather than wear depth alone [16]. Kulkarni et al. investigated the effect of the nonlinearity of the equivalent conicity function on vehicle dynamic behaviour under typical service conditions [17]. These studies indicate that wheel-rail contact geometry evolution is not only a wear problem, but also a key factor affecting hunting stability, ride quality, and wheel-rail dynamic interaction. These efforts have provided a theoretical basis for predicting the long-term in-service performance of railway vehicles. From the perspective of maintenance-oriented performance preservation, wheel-rail contact-geometry degradation is usually addressed by restoring or modifying the wheel-rail profile state. Ye et al. developed an individualised wheel profile fine-tuning system for profile recommendation [18], while Cui et al. optimised rail profiles and grinding patterns in curved subway sections [19]. With the development of condition-based maintenance, H-Nia et al. demonstrated that wheel and

rail life prediction can support maintenance decision-making for wheel-rail systems [20]. These studies mainly improve long-term service performance by intervening in wheel or rail profiles. In contrast, the present study focuses on vehicle-side dynamic adaptation to contact-geometry evolution. By adjusting the yaw-damper configuration according to the equivalent conicity state, the proposed method aims to reduce the dependence of vehicle dynamic performance on a narrow range of wheel-rail contact geometries, thereby mitigating performance degradation before profile restoration becomes necessary. Therefore, the maintenance relevance of this work lies in its potential to extend the allowable wheel service mileage and reduce premature profile-maintenance interventions. Concurrently, it has become a prevailing trend in recent years to holistically balance wear performance and operational stability by optimising wheel-rail profiles, tuning suspension parameters, and developing high-performance dampers. Specifically, Firlik et al. optimised a tram wheel profile using a biologically inspired algorithm [21], Ye et al. proposed a rotary-scaling fine-tuning method for optimising railway wheel profiles and applied it to a locomotive [22], and Qi et al. optimised the wheel profile of variable gauge high-speed trains [23]. In terms of suspension design, Li et al. optimised suspension parameters for high-speed trains with severe tread wear [24], Song et al. adopted a surrogate-model-based multi-parameter optimisation method to improve vehicle dynamics and reduce wheel wear [25], and Li et al. investigated suspension-parameter matching of high-speed locomotives based on stability/comfort Pareto optimisation [26]. In addition, Zhang et al. studied the adaptive stability mechanism of a high-speed train employing a parallel inerter yaw damper [27], and Stichel et al. discussed the potential of active suspension for improving rail vehicle dynamic performance [28]. However, the introduction of new profiles necessitates extensive long-term operational validation, and system-wide rail replacement exhibits low feasibility alongside prolonged implementation cycles. Furthermore, existing parameter optimisation studies are predominantly based on specific profiles or static contact conditions, while the deployment of complex high-performance damping devices often poses risks to overall system reliability. Consequently, achieving dynamic adaptation between vehicle dynamic performance and the evolving wheel-rail contact geometry throughout the entire life cycle in a cost-effective and highly reliable manner remains challenging in practical engineering.

To address the aforementioned engineering challenges, this paper proposes a supervisory staged configuration method for yaw dampers based on the state of wheel-rail contact geometry. First, by integrating measured wheel-rail profiles with dynamic analyses, this study identifies typical stability degradation characteristics and their corresponding contact geometry characteristics, thereby elucidating the underlying mechanisms of vehicle instability under both low and high equivalent conicity conditions. Subsequently, a linear dynamic model of the locomotive is established. Root locus analysis is then used to identify key suspension parameters affecting hunting stability under different equivalent-conicity levels, providing the basis for stability-oriented parameter matching. Furthermore, to overcome the limitation that fixed suspension parameters cannot adapt to the continuous evolution of wheel-rail matching states, a preventive staged configuration strategy is constructed. This strategy utilises the nominal equivalent conicity as a state criterion to implement staged switching of yaw damper characteristics at discrete mileage intervals. Finally, in conjunction with full-life-cycle wheel wear simulations, the evolution laws of tread profiles, equivalent conicity, and dynamic performance under different configuration schemes are systematically compared. This enables a comprehensive evaluation of the

proposed method's effectiveness regarding wear control, wheel-rail matching state preservation, and the maintenance of long-term dynamic performance, thereby validating its adaptability to wheel-rail contact geometry evolution.

The main contributions of this study are as follows. Wheel wear evolution, variations in wheel-rail contact geometry, degradation of hunting stability, and adjustments in yaw damper configuration are incorporated into a unified analytical framework, within which the parameter and configuration design of the suspension system for high-speed locomotives is discussed from a full-life-cycle perspective. In addition, a supervisory staged configuration strategy based on wheel-rail contact geometry states is proposed, providing a new perspective for the prevention of wear-induced hunting instability and state-dependent suspension system regulation of high-speed locomotives during service.

The structure of this paper is organised as follows. Section 2 analyses typical stability degradation phenomena and their corresponding wheel-rail contact geometric characteristics, reveals the relationship between wheel-rail matching states and hunting stability, and identifies the key suspension parameters based on a linear locomotive model. Section 3 performs suspension parameter optimisation based on a model-data synergy surrogate model and incorporates the equivalent conicity observer into the supervisory staged configuration framework for yaw dampers. Section 4 compares and analyses the wear evolution, variations in wheel-rail matching states, and dynamic performance evolution under different schemes through full-life-cycle wheel wear simulations. Finally, Section 5 summarises the main conclusions and provides an outlook for future work.

2. Hunting stability characteristics and root locus analysis

2.1. Hunting stability characteristics

To clarify the relationship between the two types of hunting instability observed during service and wheel-rail contact geometry, measurements of the wheel profiles and the rail profiles in the operating sections were carried out for vehicles exhibiting primary hunting and secondary hunting, respectively. The measurements showed that the rails along the line did not exhibit severe wear. Therefore, the standard CN60 rail profile was uniformly adopted in this study. The vehicle exhibiting primary hunting was equipped with a newly reprofiled JM3 wheel. Since the reprofiling standard for JM3 wheels is not unique, this reprofiled profile is denoted as $JM3_{T1}$; unless otherwise specified, it is used as the initial wheel profile in the subsequent analysis. The wheel associated with secondary hunting had accumulated a service mileage of more than 20,000 km and exhibited pronounced hollow wear; this profile is denoted as $JM3_{W}$.

The measured wheel and rail profiles were imported into the SIMPACK multibody dynamics model to update the wheel-rail contact relationship. Figure 1 shows the relationships among wheel profile characteristics, wheel-rail contact states, and dynamic responses for the two hunting instability modes, together with comparisons between measured and simulated results. Figures 1(a and b) present the wheel-rail contact geometries corresponding to primary hunting and secondary hunting, respectively, where different colours denote the contact point positions associated with different wheelset lateral displacements, Δy. Figure 1(c–f) shows the simulated and measured responses of the two hunting phenomena in the frequency and time domains.

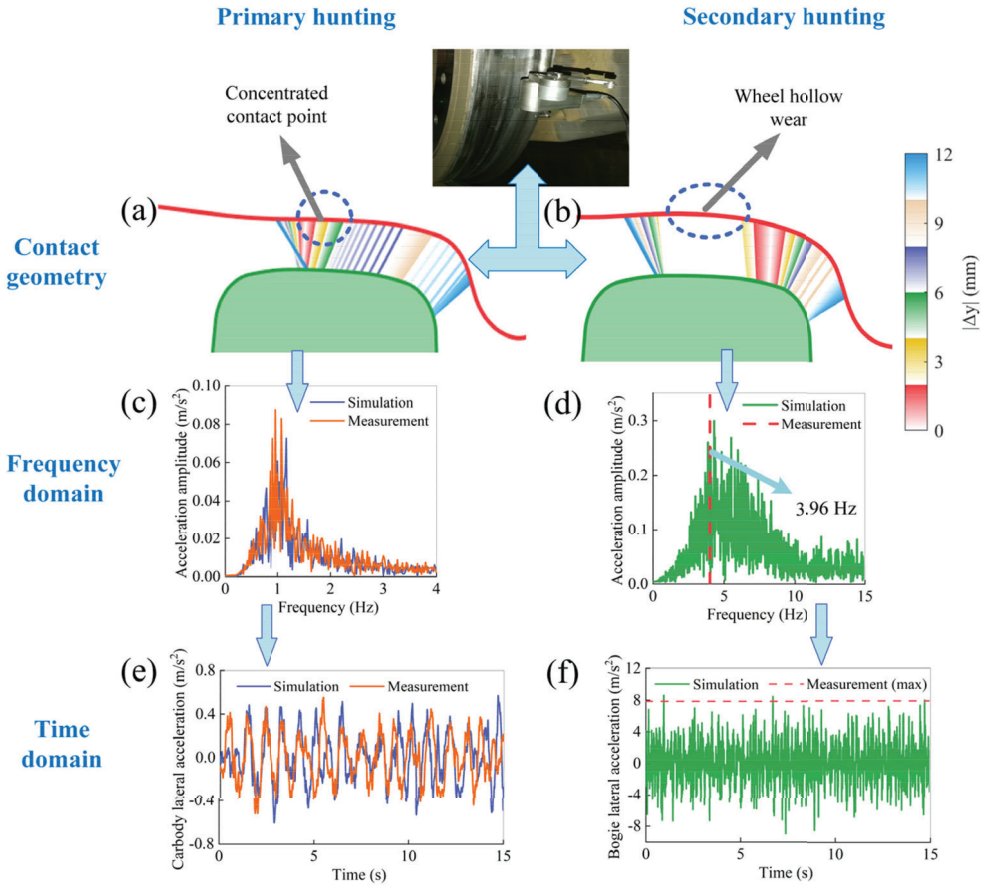


Figure 1. Field-simulation comparison of primary/secondary hunting induced by typical wheel-rail profile degradation.

As shown in Figure 1(a), when $JM3_{T1}$ is matched with the rail profile, a pronounced concentration of contact points appears, and the contact region is located on the side away from the flange, resulting in a smaller rolling radius difference induced by wheelset lateral displacement. In contrast, Figure 1(b) shows that, after wear, the contact points shift toward the flange side when the wheel is matched with the rail profile, leading to a larger rolling radius difference caused by wheelset lateral displacement. As can be seen from Figure 1(c–f), primary hunting is mainly characterised by low-frequency swaying reflected in the carbody lateral acceleration, whereas secondary hunting is mainly manifested as higher-frequency vibration represented by the bogie lateral acceleration. The simulation results agree well with the measurements in terms of the dominant frequency band in the frequency domain and the amplitude characteristics in the time domain, thereby confirming that the evolution of wheel-rail contact geometry is the key factor inducing these two types of hunting instability.

The influence of wheel-rail contact geometry on hunting stability can be interpreted through the rolling-radius difference function. Lateral displacement of a wheelset changes the left and right contact positions, producing a rolling-radius difference that generates a

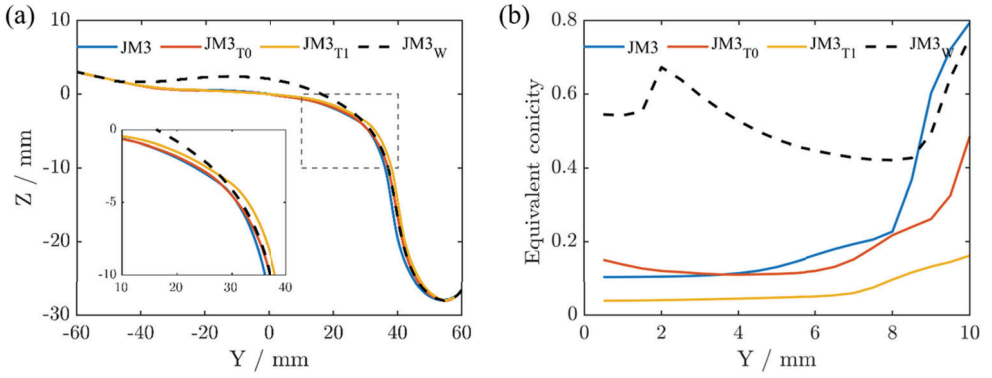


Figure 2. Comparison of four typical wheel tread profiles and the corresponding equivalent conicity characteristics when matched with the standard rail: (a) comparison of four wheel tread profiles; (b) equivalent conicity curves of the four tread profiles matched with the standard rail.

yawing moment and couples lateral and yaw motions. This mechanism normally provides self-centering, but a larger rolling-radius difference strengthens the coupling and increases the hunting frequency. Equivalent conicity characterises the overall variation of the rolling-radius difference within a given lateral displacement range and serves as a key indicator of the wheel-rail matching state. Higher equivalent conicity generally lowers the critical speed and may induce high-frequency secondary hunting instability, whereas excessively low equivalent conicity tends to cause low-frequency primary hunting instability.

Figure 2 presents the wheel tread profiles under four tread conditions and the corresponding comparisons of equivalent conicity when matched with the standard rail. The four tread conditions include the standard JM3 tread, two thin-flange treads with different flange thicknesses, denoted as $JM3_{T0}$ and $JM3_{T1}$, and the worn tread $JM3_{W}$.

As shown in Figure 2(a), noticeable differences can be observed among the four tread profiles in the flange region and the tread transition region. Figure 2(b) further shows that these profile differences lead to significant changes in the wheel-rail matching relationship, which are ultimately reflected in the equivalent conicity curves. Specifically, $JM3_{T1}$ exhibits an extremely low equivalent conicity, whereas $JM3_{W}$ exhibits an extremely high equivalent conicity. These results indicate that the evolution of wheel tread morphology can significantly alter the wheel-rail contact geometry and further affect the hunting stability of the vehicle.

2.2. Linear dynamic model

To analyse the mechanisms and influencing factors of hunting stability and identify the key suspension parameters, nonlinear factors such as wheel-rail contact and dampers were linearised, and a simplified linear dynamic model was established. A schematic of the linear model is shown in Figure 3. The model is described in the carbody coordinate system *O-xyz*, in which the positive x-axis points toward the front of the locomotive, the positive y-axis points to the right in the top view, and the positive z-axis is defined downward from the centre of mass. The vehicle system consists of the carbody, bogies, wheelsets, motors,

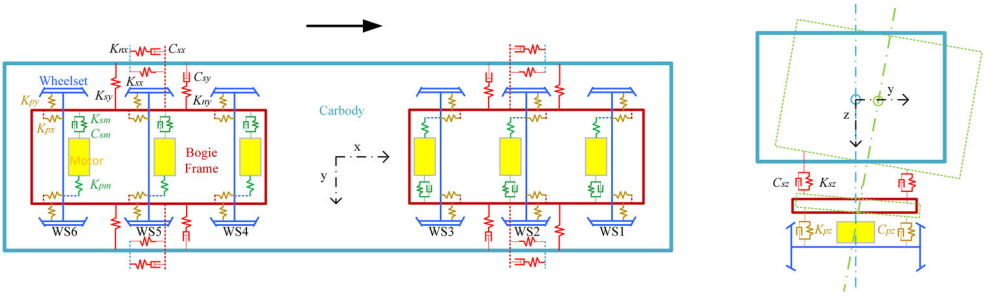


Figure 3. Simplified linear dynamic model of the locomotive.

and suspension elements. The suspension elements include the primary suspension, secondary suspension, and motor suspension, which are represented by brown, red, and green symbols, respectively, in Figure 3.

The lateral damper in the secondary suspension and the yaw damper are modelled using Maxwell elements, whereas all other suspension components are represented by Kelvin-type spring-damper elements. To highlight the mechanism of hunting stability and lateral vibration, only the lateral displacement and yaw degrees of freedom (y_w, ψ_w) are retained for the wheelsets, while the bogie frames and the carbody retain the lateral displacement, yaw, and roll degrees of freedom (y, ψ, ϕ), and the motors retain only the lateral degree of freedom (y_d). Accordingly, the generalised coordinate vector q is defined as shown in Equation (1).

$$q = [y_{w1}, \psi_{w1}, \cdots, y_{w6}, \psi_{w6}, y_{f1}, \phi_{f1}, \psi_{f1}, \cdots, y_c, \phi_c, \psi_c, y_{d1}, \cdots, y_{d6}]^T \tag{1}$$

Here, the subscripts *w, f, c,* and *d* denote the wheelset, bogie frame, carbody, and motor, respectively. Under the assumptions of small displacements and small rotation angles, the relative displacements between the mounting points at both ends of each suspension element can be expressed as linear combinations of the generalised coordinates.

The dynamic equations are formulated based on the relative deformations of the suspension elements and are automatically assembled through global matrices. For an arbitrary suspension element j, its relative deformation can be expressed as

$$\delta_j(q) = a_j^{\mathsf{T}} q \tag{2}$$

where, a_j is a sparse coefficient vector determined by the geometric positions of the mounting points, and this representation compactly incorporates the geometric coupling into a_j.

For the Kelvin-type (parallel) spring-damper elements, based on the principle of virtual work, their assembly forms into the global stiffness and damping matrices can be expressed as:

$$K \leftarrow K + k_j a_j a_j^{\mathsf{T}}, \qquad C \leftarrow C + c_j a_j a_j^{\mathsf{T}} \tag{3}$$

An internal state variable, z_j, is introduced to represent the deformation of the internal spring branch within the Maxwell model. According to its series structural characteristics and force equilibrium conditions, the element force and the internal state differential

equation can be derived as follows:

$$F_j = k_j z_j, \dot{z}_j = a_j^T \dot{q} - \frac{k_j}{c_j} z_j \tag{4}$$

By stacking the geometric coefficient vectors of all Maxwell elements into the matrix $A_m = [a_1, \ldots, a_m]$, and defining

$$K_s = \mathrm{diag}(k_1, \ldots, k_m),\ D = \mathrm{diag}(k_1/c_1, \ldots, k_m/c_m) \tag{5}$$

the system dynamic equations with internal states can be obtained as

$$M\ddot{q} + C_0\dot{q} + K_0 q + A_m K_s z = Q_{wr}, \dot{z} = A_m^{\mathrm{T}}\dot{q} - Dz \tag{6}$$

where, K_0 and C_0 denote the contributions of all structural and suspension components other than the Maxwell elements to the system stiffness and damping, respectively. Wheel-rail contact is modelled using linear creep theory, and its effect is incorporated into the system equations through the equivalent linear force term Q_{wr}.

The augmented state vector $x$is defined as shown in Equation (7).

$$x = [q^{\mathrm{T}}, \dot{q}^{\mathrm{T}}, z^{\mathrm{T}}]^{\mathrm{T}} \tag{7}$$

Based on Equation (6), the system dynamic equations can be equivalently reformulated into a linear time-invariant state-space form by introducing the augmented state vector, as follows:

$$\dot{x} = \underbrace{\begin{bmatrix} 0 & I & \\ -M^{-1}K & -M^{-1}C & -M^{-1}A_m K_s \\ 0 & A_m^{\mathrm{T}} & -D \end{bmatrix}}_{A} x \tag{8}$$

The modal damping and frequency characteristics can be obtained by calculating the eigenvalues, denoted as $\lambda = \sigma \pm j\omega$, of the system matrix A. Here, σ and ω represent the real and imaginary parts of the eigenvalue, respectively. The modal frequency f and damping ratio ζ can be expressed as follows:

$$f = \frac{\omega}{2\pi}, \zeta = -\frac{\sigma}{\sqrt{\sigma^2 + \omega^2}} \tag{9}$$

By sweeping key parameters such as the running speed and equivalent conicity, the evolution laws of the system modes with respect to these parametric variations can be systematically analysed.

2.3. Root locus analysis

The root locus of the linear model provides an intuitive evaluation of the locomotive's stability margin and its evolution laws with respect to parameter variations. To facilitate the accurate identification of the physical attributes of distinct modes in the root locus plot, the

modes are labelled based on the modal energy distribution of the eigenvectors. The potential energy component associated with the i-th degree of freedom (DOF) is expressed as follows:

$$E_{p,i} = \frac{1}{2} Re\{\bar{\phi}_i (K\phi)_i\} \tag{10}$$

where K is the stiffness matrix and ϕ is the displacement modal vector. The potential energy share of the i-th DOF is defined in Equation (11):

$$EpShare_i = \frac{E_{p,i}}{\sum_j E_{p,j}} \tag{11}$$

To rapidly identify the physical origins of different modes in the root locus plot, the modal potential energy share, EpShare_i, serves as the classification criterion. Specifically, the DOF exhibiting the maximum EpShare_i is defined as the dominant DOF of that mode, allowing the eigenvalues to be classified and labelled accordingly. Figure 2 illustrates the root loci under speed-sweeping conditions for three equivalent conicity scenarios ($\lambda =$ 0.04, 0.16, 0.60). In this plot, different colours are utilised to distinguish the equivalent conicities, while the marker sizes correspond to the running speeds.

In Figure 4, the horizontal axis represents the modal damping ratio ζ, and the vertical axis represents the damped modal frequency f. Each root locus curve consists of 45 sets of eigenvalues, corresponding to a speed sweep from 80 to 300 km/h. In theory, the system becomes unstable when the damping ratio falls below zero. However, from a more conservative engineering perspective, a threshold of 0.05 is adopted in this study. The two green dashed lines in the figure denote the theoretical instability threshold and the engineering instability threshold, respectively.

As shown in Figure 4, the carbody-related modes are mainly distributed in the low-frequency range. Under low-conicity conditions, the frequencies of the hunting-related modes decrease and move closer to the carbody modes, indicating a more pronounced coupling trend. Under high-conicity conditions, by contrast, the frequencies of the hunting-related modes shift upward, and the distribution of the modal clusters differs significantly from that under low-conicity conditions.

Given the clear differences in hunting stability characteristics under high- and low-conicity conditions, the influence of suspension parameters on stability is further analysed. A total of 12 suspension parameters are selected as variables, and their symbols and ranges are listed in Table 1.

In Table 1, the secondary longitudinal stiffness and the secondary lateral stiffness are assigned the same range of values. Therefore, only the secondary longitudinal stiffness is used in this study to represent both parameters. The 12 suspension parameters listed in Table 1 are each uniformly discretized into 40 sampling points within their prescribed ranges, and the corresponding root loci are calculated one by one under three equivalent conicity conditions. The results are shown in Figure 5.

As shown in Figure 5, the primary longitudinal stiffness, yaw damper damping, secondary lateral damper damping, yaw damper stiffness, secondary vertical stiffness, and secondary longitudinal stiffness have significant influences on stability. Considering both the operational feasibility in maintenance practice and the degree to which suspension

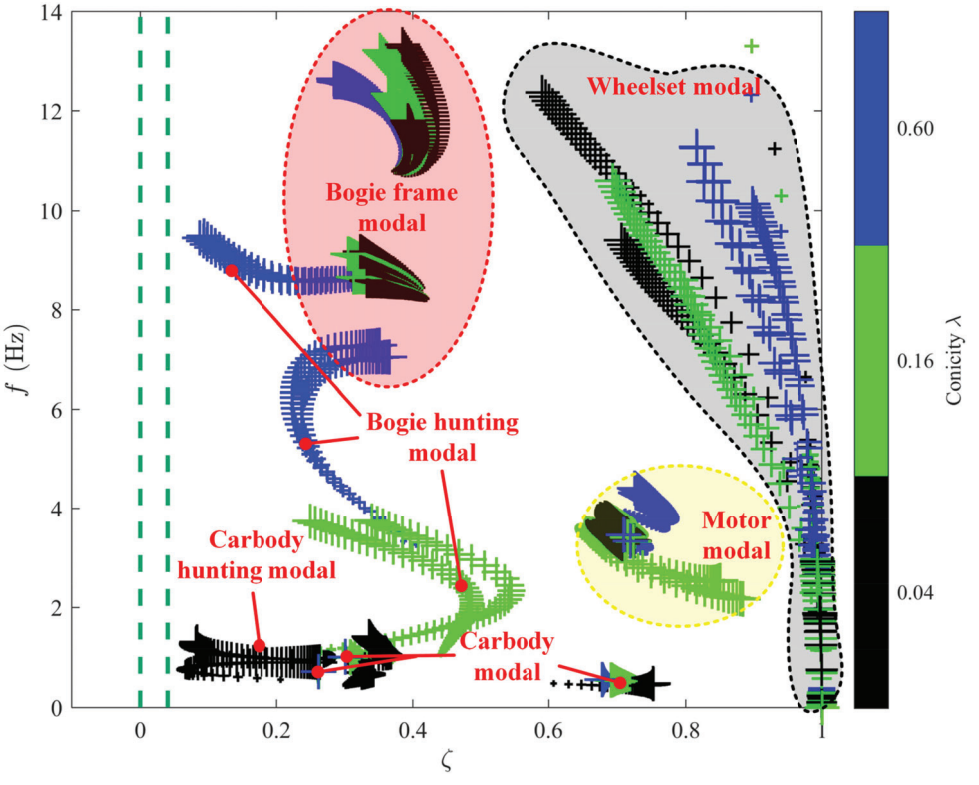


Figure 4. Root loci and modal classification under a speed sweep for different equivalent conicities.

Table 1. Suspension parameters considered in the analysis and their ranges, baseline values, units, and symbols.

Suspension parameter	Range	Original value	Unit	Symbol	Order
Primary longitudinal stiffness	17.1 ~ 51.3	34.2	kN/mm	*Kpx*	a
Primary lateral stiffness	2.5 ~ 7.5	5.1	kN/mm	*Kpy*	b
Primary vertical stiffness	1.07 ~ 3.21	2.154	kN/mm	*Kpz*	c
Yaw damper damping (single)	250 ~ 750	500	kN·s/m	*Csx*	d
Secondary lateral damper damping	30 ~ 90	50	kN·s/m	*Csy*	e
Secondary vertical damper damping	5 ~ 15	10	kN·s/m	*Csz*	f
Yaw damper stiffness (single)	4 ~ 12	8	kN/mm	*Knx*	g
Secondary lateral damper stiffness	6.25 ~ 18.75	12.5	kN/mm	*Kny*	h
Secondary vertical stiffness	0.55 ~ 1.65	1.11	kN/mm	*Ksz*	i
Secondary longitudinal stiffness	0.165 ~ 0.495	0.33	kN/mm	*Ksx*	j
Motor mounting stiffness	0.6 ~ 1.8	1.2	kN/mm	*Ksm*	k
Motor mounting damping	40 ~ 120	80	kN·s/m	*Csm*	l

parameters affect stability, the yaw damper is selected as the adjustment target. A supervisory damping scheduling strategy based on equivalent conicity is therefore proposed to realise the staged configuration of the yaw damper. Using equivalent conicity as an indicator of the wheel-rail contact geometry state, when the observed equivalent conicity exceeds a preset threshold, the yaw damper configuration is switched from single-damper operation to dual-damper operation to enhance hunting stability. After wheel reprofiling, when the equivalent conicity returns to a low level, the configuration is switched back from

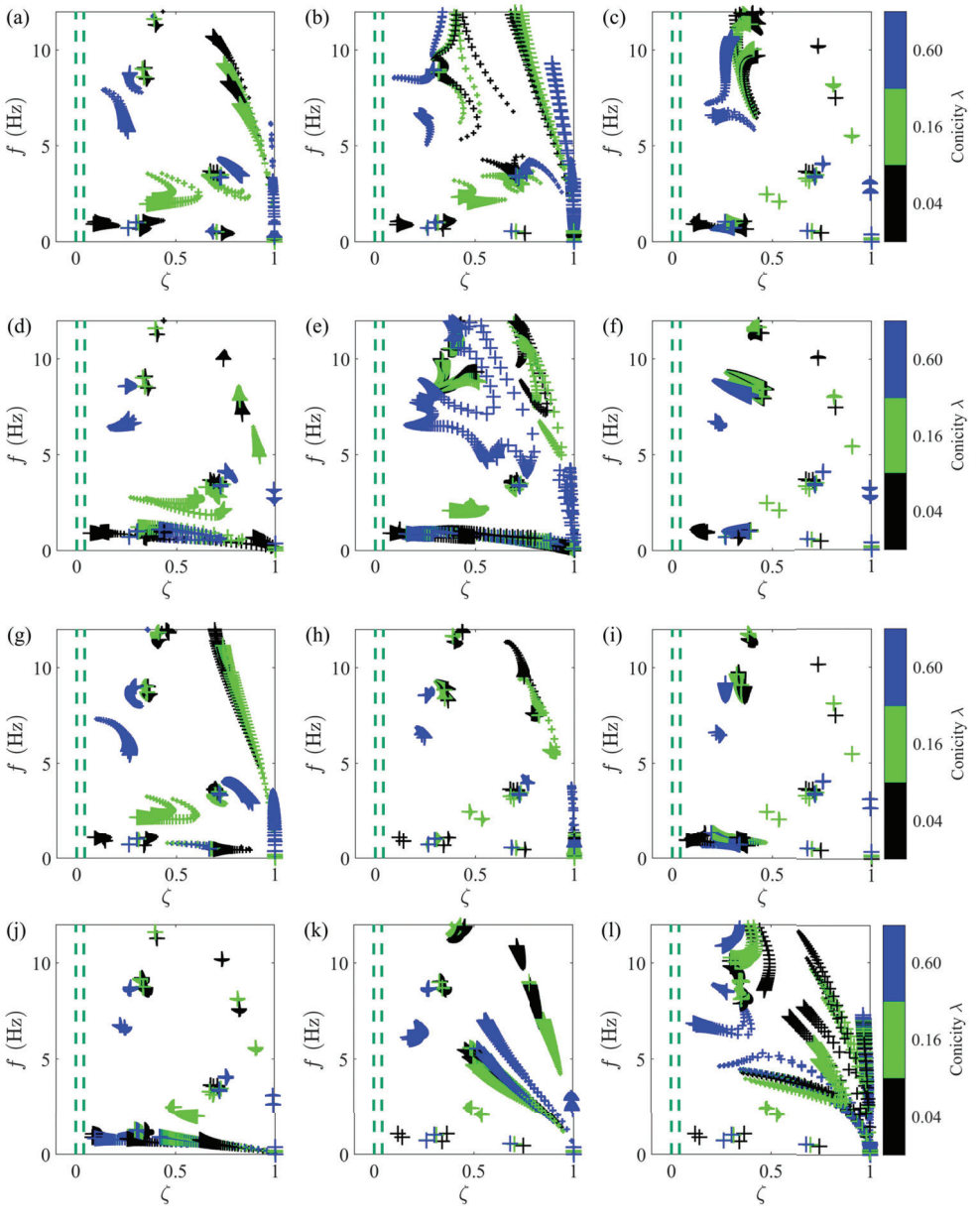


Figure 5. Root-locus responses and comparative influence analysis under parameter sweeps for different equivalent conicities.

dual-damper operation to single-damper operation so as to improve ride comfort. Within one wheel reprofiling cycle, this strategy typically requires only one manual adjustment, which can be implemented by tuning the damping valve knob of the yaw damper. Based on the root locus analysis of the single- and dual-yaw-damper configurations, and considering both stability improvement and practical implementation, the equivalent conicity threshold was set to 0.1 in this study.

3. Staged configuration strategy for yaw dampers

Existing suspension parameter schemes are usually designed under the assumption of a fixed yaw damper configuration. In this study, a staged yaw damper strategy is introduced, allowing the configuration to switch with changes in the wheel-rail contact state, thereby altering the dynamic characteristics of the vehicle system and the associated parameter matching relationship. Therefore, suspension parameter optimisation needs to be revisited within this strategy framework. Meanwhile, since equivalent conicity is difficult to measure directly in service but is closely correlated with vehicle dynamic responses, it can be indirectly observed from operational monitoring data. Accordingly, this chapter discusses suspension parameter optimisation and equivalent conicity observation under the staged strategy.

3.1. Suspension parameter optimization based on the staged yaw damper strategy

Based on the results presented in Section 2, six suspension parameters were selected as the optimisation variables. To ensure the reliability of the optimisation results, the SIMPACK multibody dynamics model was employed as a high-fidelity evaluator to assess the dynamic performance of candidate parameter combinations under unified operating conditions. The accuracy of this model has been validated in previous studies [29].

3.1.1. Modelling of multi-condition objective functions and constraints

In multi-objective optimisation, there is generally no unique optimal solution; instead, a set of non-dominated compromise solutions is obtained, whose mapping in the objective space constitutes the Pareto front. Subject to the dynamic constraints, the suspension parameters are optimised within their prescribed ranges to obtain the Pareto-optimal compromise solution set for dynamic performance.

Based on the dynamic characteristics of primary and secondary hunting, the dynamic performance indices considered in this study include wheelset lateral force on a long straight track, wear performance, bogie lateral acceleration, and ride comfort. Among them, the wheelset lateral force F_{EN} and the bogie lateral acceleration A_{EN} are mainly used to characterise secondary hunting stability, and their evaluation is based on the European standard EN 14363 [30]. The lateral axle box force and the bogie-frame lateral acceleration were processed using a band-pass filter with a passband of $f_0 \pm 2$ Hz, where f_0 denotes the dominant frequency under unstable running conditions. Additionally, a sliding root mean square (RMS) method was applied, with a window length of 100 m and a step length not exceeding 10 m. For the locomotive considered in this study, the instability limits are 32.8 kN and 3.9 m/s^2 for the wheelset lateral force and bogie-frame lateral acceleration, respectively.

A wear number index (WNI) is introduced to characterise wear performance, and is defined as follows:

$$WNI = \frac{1}{t_e - t_s} \int_{t_s}^{t_e} (T_x \gamma_x + T_y \gamma_y) dt \tag{12}$$

where T_x is the longitudinal creep force, T_y the lateral creep force, γ_x the longitudinal creepage, γ_y the lateral creepage, t_s the simulation start time and t_e the end time. The Sperling

Table 2. Four dynamic indicators and their maximum deviation coefficients.

Objective symbol	λ (max-deviation coefficient)	Original unit	Description
F_{EN}	0.4	kN	Wheelset lateral force
WNI	0	N	Wear number index
A_{EN}	0.4	m/s^2	Bogie-frame lateral acceleration
W_y	0.6	Dimensionless	Sperling lateral ride comfort index

index is used to quantify lateral ride comfort and is therefore adopted to evaluate primary hunting stability [31]. It is defined as follows:

$$W_y = 3.57 \sqrt[10]{\frac{{A_y}^3}{f} F_y(f)} \tag{13}$$

where A_y is the lateral acceleration amplitude in the frequency domain, f is the corresponding frequency, and $F_y(f)$ is the frequency correction coefficient. For passenger vehicles, the limit values of ride comfort are 2.5, 2.75, and 3.0 for excellent, medium and qualified levels, respectively. Generally speaking, the excellent level is required during vehicle operation [1].

Five typical wheel–rail contact conditions were selected, with nominal equivalent conicities of 0.05, 0.11, 0.32, 0.48, and 0.68, respectively, to represent the differences in contact geometry at different wear stages. For each set of suspension parameters, the dynamic performance indices were evaluated under all five conditions. To account for robustness across multiple operating conditions without increasing the dimensionality of the objective space, and to facilitate result analysis, a multi-condition aggregation approach was adopted to map the responses of each dynamic index under the five conditions into a single scalar objective. In this aggregation form, a penalty for the deviation associated with the most unfavourable condition is introduced in addition to the mean term. The resulting multi-condition aggregated objective is defined as follows:

$$\mathbf{J} = \mu + \lambda \Lambda \tag{14}$$

where μ denotes the mean value, Δ represents the maximum deviation, and λ is the maximum deviation coefficient, which reflects the degree of emphasis placed on the most adverse operating conditions for the given indicator. The specific values of the maximum deviation coefficients for the four dynamic indicators are listed in Table 2.

The maximum deviation coefficients in Table 2 define the penalty weights for unfavourable operating conditions. For WNI, which mainly reflects long-term accumulated wear, the mean value is more important than the peak under a single condition, so its coefficient is set to 0. For F_{EN} and A_{EN}, which are related to running safety, vehicle loading, and fatigue risk, a balanced coefficient of 0.4 is used. For W_y, which directly affects ride comfort and service quality, a higher coefficient of 0.6 is adopted to penalise deterioration under individual conditions.

To eliminate the dimensional and magnitude differences among various dynamic indicators and to facilitate the horizontal comparison of multi-objective results, the aggregated objectives are further normalised. Assuming the decision vector of the baseline scheme (original suspension parameters) is denoted as $\mathbf{x}_0$, and its aggregated objective obtained

under the same evaluation procedure and the five-condition set is $\mathbf{J}(\mathbf{x}_0)$, the normalised objective for any candidate suspension parameter vector $\mathbf{x}$ is defined as follows:

$$\tilde{\mathbf{J}}(\mathbf{x}) = \frac{\mathbf{J}(\mathbf{x})}{\mathbf{J}(\mathbf{x}_0)} \tag{15}$$

Consequently, the core of the optimisation problem lies in finding the optimal design values for the decision vector $\mathbf{x}$ within the lower bound lb and upper bound ub, in order to minimise the objective functions listed in Table 2. Simultaneously, curve negotiation safety criteria must be satisfied: the state coefficient is set to $S_c = 1$ if the safety conditions are met [30], and $S_c = 0$ otherwise. In summary, the multi-objective optimisation problem can be formulated as follows:

$$\begin{cases} \text{Minimize: } \tilde{\mathbf{J}}(\mathbf{x}) = \{F_{\text{EN}}(\mathbf{x}), \text{WNI}(\mathbf{x}), A_{\text{EN}}(\mathbf{x}), W_y(\mathbf{x})\} \\ \text{Find: } \mathbf{x} = [Kpx, Csx, Csy, Knx, Ksz, Ksx]^{\text{T}} \\ \text{Subject to: } S_c(\mathbf{x}) = 1, lb \leq \mathbf{x} \leq ub \end{cases} \tag{16}$$

3.1.2. Construction of the model-data synergy surrogate model

The diversity of wheel-rail contact and the iterative optimisation of suspension parameters make direct global search with the high-fidelity SIMPACK model computationally expensive. To improve efficiency, a model–data synergy surrogate modelling framework is adopted, as shown in Figure 6. Measured wheel and rail profiles are used to represent contact geometry states, and offline SIMPACK simulations are performed to generate training samples. The surrogate model then maps wheel-rail geometry and suspension parameters to dynamic performance indices. During optimisation, it is used for rapid evaluation, while selected candidates are rechecked using the high-fidelity model.

In the sample construction stage (upper-left panel of Figure 6), a hybrid sampling strategy combining regular DOE sampling and Hammersley-sequence augmentation is adopted. DOE ensures baseline coverage of the design space, while the Hammersley sequence improves sample uniformity. Redundant samples are removed using a minimum-distance criterion. SIMPACK simulations are then performed for the selected inputs X to obtain outputs Y, forming a dataset (X,Y) with 10^5 samples. The inputs include wheel–rail geometric states and suspension parameters, and the outputs include four straight-track dynamic indices and the curve-negotiation feasibility indicator S_c.

In the surrogate-model training stage (right panel of Figure 6), a combined classification-and-regression structure is adopted. First, a feasibility classifier is trained to determine whether the curve negotiation safety constraint is satisfied. Then, based on the feasible samples, four regression surrogate models are established to predict different dynamic performance indices. The regression part uses LSBoost (least squares boosting), a decision-tree-based ensemble method, to approximate the target functions by iteratively adding weak learners. Specifically, at the m-th iteration, a regression tree $h_m(x)$ is trained using the residual

$$r_m = y - F_{m-1}(x) \tag{17}$$

and the model is updated with learning rate ηas

$$F_m(x) = F_{m-1}(x) + \eta h_m(x) \tag{18}$$

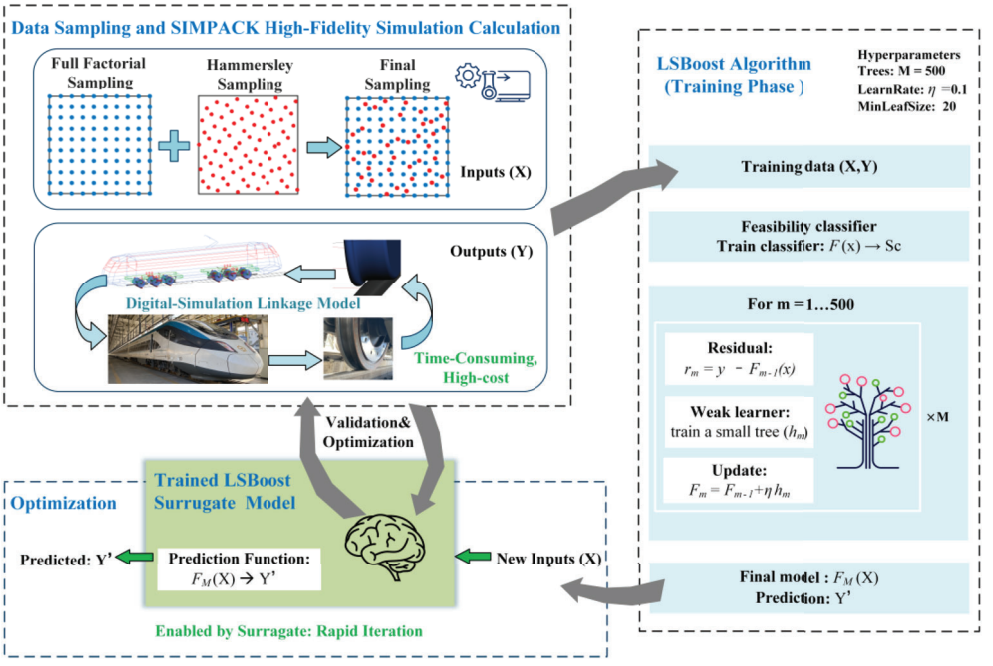


Figure 6. Model-data synergy LSBoost surrogate modelling framework for hybrid sampling, surrogate training, and optimisation with high-fidelity validation.

After M iterations, the final model $F_M(x)$is obtained. In this study, $M = 500$, $\eta = 0.1$, and the minimum leaf size is set to 20 (MinLeafSize $= 20$).

In the validation and optimisation stage (lower-left panel of Figure 6), the surrogate model is used in place of the high-fidelity model for rapid evaluation and iterative search over a large number of candidate solutions. Meanwhile, several representative candidate solutions or Pareto-front points are re-evaluated in SIMPACK to verify the consistency between the surrogate predictions and the high-fidelity results. When necessary, these validated samples are fed back into the training dataset to further improve the reliability of the surrogate model.

After the surrogate model was trained, 200 suspension parameter combinations were randomly sampled within the prescribed parameter ranges for both dynamic simulations and surrogate-model predictions. The results show that the coefficients of determination for all dynamic performance indices are greater than 0.99, thereby confirming the high predictive accuracy of the surrogate model.

3.1.3. Pareto front analysis and scheme comparison

Based on the LSBoost surrogate model, a hybrid evolutionary framework (GA–PSO) is used to solve the multi-objective suspension-parameter optimisation problem. The Pareto front of the four objectives, expressed in terms of aggregated and normalised metrics, is shown in Figure 7. The three axes correspond to the wheelset lateral force F_{EN}, the wear number index (WNI), and the lateral ride comfort index W_y, respectively. The colour map indicates the lateral acceleration of the bogie frame, A_{EN}, where darker colours correspond

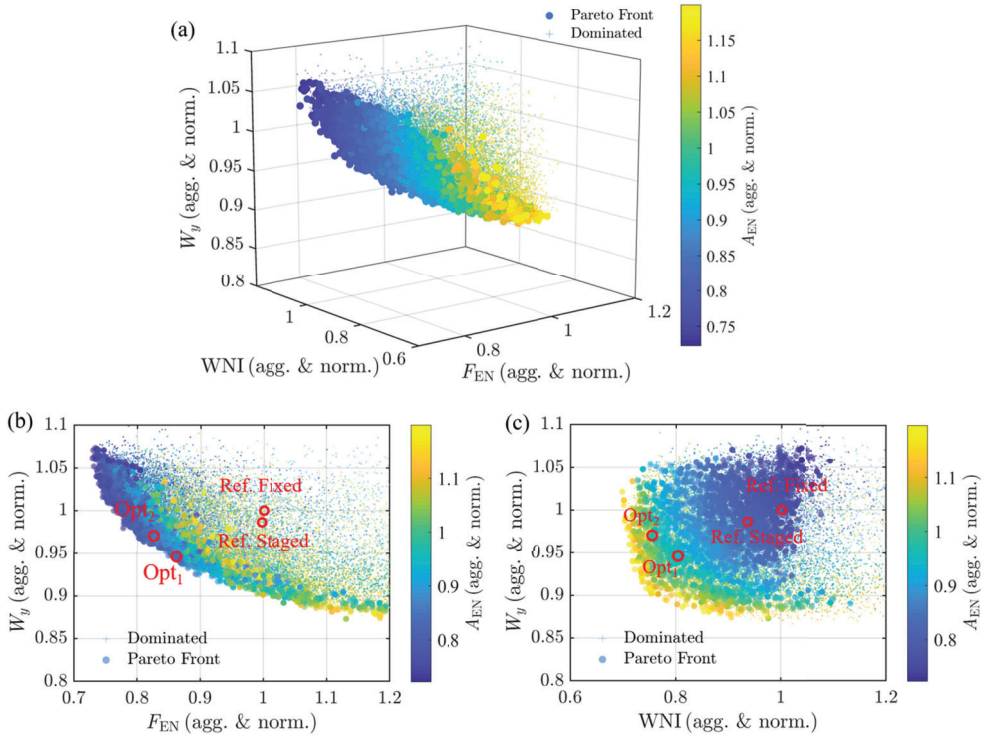


Figure 7. Pareto front of aggregated and normalised objectives: (a) F_{EN}-W_y plane; (b) WNI-W_y plane.

to lower values. Dominated solutions are marked with the symbol '+' to provide a visual contrast with the Pareto-front solutions and thereby enhance the presentation of the front.

The obtained Pareto front clearly reveals the trade-offs among the objectives, and the suspension-parameter set can be selected from the non-dominated solutions according to specific design preferences. To support decision making and extract representative designs from the Pareto set, a weighted-sum scalarization is adopted to combine the four normalised objectives into a single composite score. It should be noted that the weighting coefficients are not used to generate the Pareto front, but only to identify representative solutions from the obtained non-dominated set according to different design preferences.

In this scalarization, the weighting coefficients are assigned after normalisation of all objectives; therefore, they represent relative design preferences rather than dimensional scaling factors. A unit weight of 1.0 was first taken as the neutral preference for each objective, so that the total coefficient sum was kept equal to 4.0 in both composite functions. This setting keeps the two scalarized objectives comparable and avoids changes in the total weight magnitude affecting the composite score. Since F_{EN} and A_{EN} are both safety-related indicators associated with running stability assessment, they were treated as a coupled stability requirement. Therefore, the total weight assigned to these two indicators was kept identical in the two preference scenarios, i.e. $0.8 + 0.8 = 1.6$, ensuring that the basic running-safety requirement was not weakened when another performance aspect was emphasised. The remaining emphasis was assigned to the application-dependent objective. For the first preference scenario, later denoted as Opt1, a larger coefficient is assigned

Table 3. Suspension parameter values of the optimised schemes.

Scheme	*Kpx* (kN/mm)	*Csx* (kN·s/m)	*Csy* (kN·s/m)	*Knx* (kN/mm)	*Ksz* (kN/mm)	*Ksx* (kN/mm)
Opt1	23.3	739.2	43.9	11.0	1.44	0.18
Opt2	19.3	738.5	55.4	10.5	1.36	0.24
Original value	34.2	500	60	8	1.11	0.33

to W_y to represent a ride-quality-oriented design, while WNI retains a secondary coefficient. For the second preference scenario, later denoted as Opt2, a larger coefficient is assigned to WNI to represent an operation-economy-oriented design associated with lower wheel wear, while the ride-quality objective retains a secondary coefficient. Therefore, the following scalarized objectives are not intended to define a universally optimal weighting scheme, but to provide two representative preference settings for extracting typical solutions from the Pareto front. Accordingly, the two composite objectives used for selecting representative solutions from the Pareto front are defined as

$$\begin{cases} Opt1 = 0.8F_{EN} + 0.8WNI + 0.8A_{EN} + 1.6W_y \\ Opt2 = 0.8F_{EN} + 1.6WNI + 0.8A_{EN} + 0.8W_y \end{cases} \tag{19}$$

Based on Equation (19), the solution with the minimum value of each composite objective is selected from the Pareto front. The two resulting optimised configurations are denoted as Opt1 and Opt2, which correspond to the preference for improved ride quality and the preference for better operational economy, respectively. In addition, two reference configurations are introduced for comparison with the optimised schemes: Ref.Fixed, which uses the original suspension parameters with a fixed yaw damper configuration, and Ref.Staged, which uses the original suspension parameters with the staged yaw damper strategy enabled. Accordingly, four configurations, namely Ref.Fixed, Ref.Staged, Opt1, and Opt2, are highlighted in Figure 7.

As shown in Figure 7, both Opt1 and Opt2 significantly improve the dynamic performance compared with the original scheme. Specifically, for Opt1, the wheelset lateral force and bogie-frame lateral acceleration are both reduced by approximately 10%, while the wear performance is improved by nearly 20%. Opt2 achieves substantial improvements in the wheelset lateral force and wear performance while causing almost no change in the ride-comfort index. Applying the staged yaw damper strategy to the original suspension parameters can also slightly improve the wear and ride-comfort indices, although the overall effect remains limited.

The specific suspension parameter values for the optimised schemes are presented in Table 3.

As shown in Table 3, the yaw damper damping and yaw damper stiffness values of Opt1 and Opt2 are very close to each other, and both are approximately 1.5 times those of the original parameter set. Compared with Opt1, Opt2 adopts a smaller primary longitudinal stiffness and a larger secondary lateral damper damping. This adjustment sacrifices part of the ride comfort in exchange for improved wear performance.

SIMPACK simulations are subsequently performed for these configurations to validate the accuracy of the surrogate predictions, with the validation results illustrated in Figure 8.

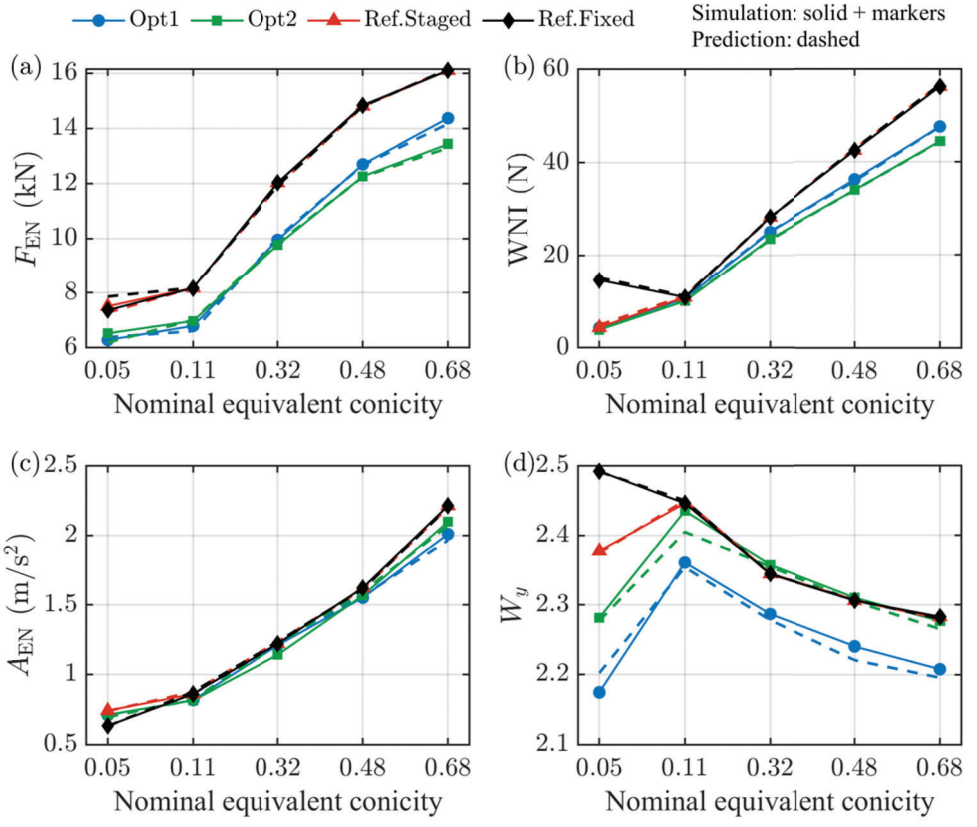


Figure 8. Validation of simulation-prediction agreement for four dynamic indicators under different nominal equivalent conicity levels.

As shown in Figure 8, the surrogate-model predictions agree well with the dynamic simulation results, further confirming the reliability of the surrogate-model-assisted optimisation results. In this study, all computations were performed on a PC equipped with Windows 10, 64 GB RAM, and an AMD 7950X processor. Under the same hardware configuration and operating conditions, direct multi-objective optimisation based on the dynamic model generally requires more than one month, whereas the surrogate-model-assisted optimisation takes approximately 2 h. This indicates that the proposed surrogate-model-assisted multi-objective optimisation method significantly improves the optimisation efficiency.

Opt1 exhibits excellent ride comfort, whereas Opt2 achieves lower wheel-rail interaction forces and better wear performance. The differences in dynamic performance among the schemes also demonstrate the effectiveness of the multi-condition aggregation method. The validated designs are used in the next section for full-life-cycle wear simulations and performance assessment.

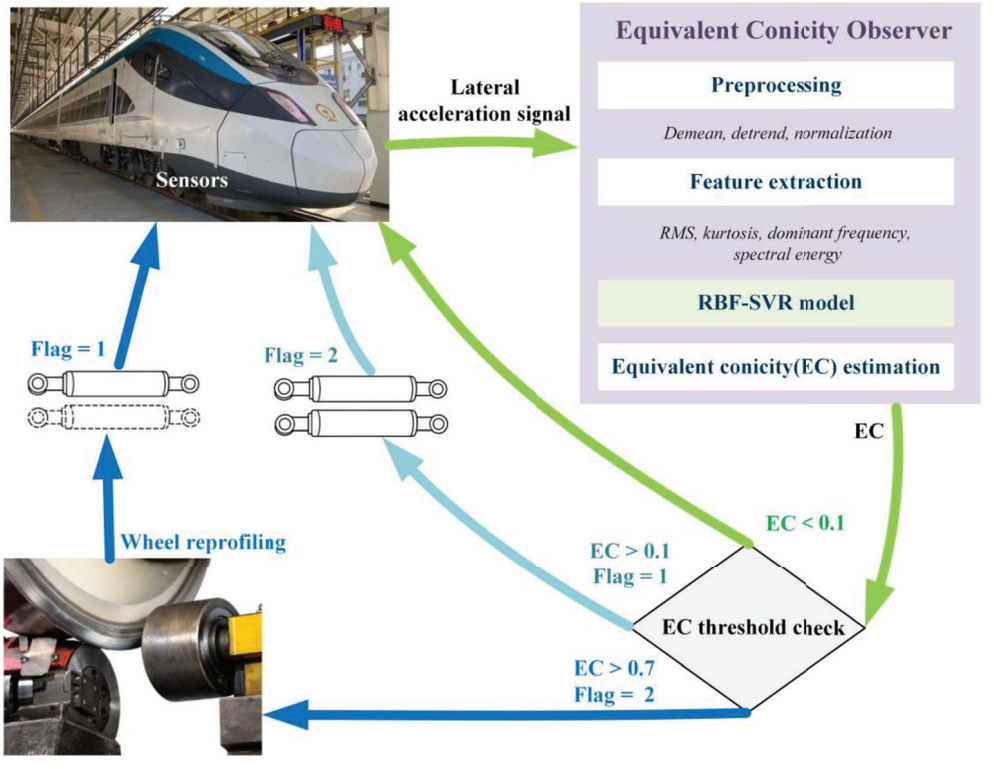


Figure 9. Closed-loop framework for yaw damper staged configuration based on equivalent conicity observation.

3.2. Equivalent conicity observation for staged configuration

Equivalent conicity characterises wheel–rail contact geometry and matching state, and its evolution directly affects vehicle dynamic performance. Compared with wear depth or tread-profile parameters, it better reflects the dynamic influence of wheel–rail matching and is therefore suitable as the criterion for staged configuration and maintenance triggering. Based on locomotive design experience and the analysis in Section 2.3, the thresholds are set to 0.1 for yaw-damper switching and 0.7 for wheel reprofiling.

Since nominal equivalent conicity cannot be measured directly during operation, axle-box lateral acceleration is used as the input of the observation model, while the corresponding nominal equivalent conicity is used as the output. An RBF-SVR-based observer is constructed to establish this mapping. Based on the observer, a closed-loop framework for staged yaw-damper configuration is established, as shown in Figure 9.

Axle-box lateral acceleration is collected and input into the equivalent-conicity observer. After demeaning, detrending, and normalisation, features including root mean square, kurtosis, dominant frequency, and band energy are extracted for online conicity estimation. The yaw-damper configuration is then adjusted according to the estimated conicity level. Once the maintenance threshold is reached, wheel reprofiling is performed to restore the tread profile, forming a closed loop among wear evolution, state identification, configuration adjustment, and profile restoration.

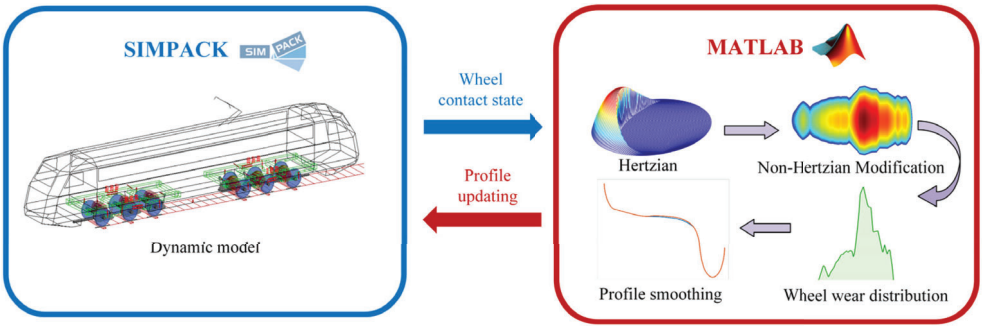


Figure 10. Framework of the full-life-cycle wheel wear simulation.

4. Full-life-cycle wheel wear simulation validation and comparative analysis of the optimised schemes

In this section, a high-fidelity wear prediction model is employed to systematically analyse the wear evolution, wheel-rail matching state, and dynamic performance variation of the four schemes obtained in Section 3 over the service mileage range, so as to validate the effectiveness of the optimised schemes.

4.1. Simulation framework and description of evaluation indices

The full-life-cycle wheel wear simulation is implemented through the joint use of SIMPACK and MATLAB, and its basic workflow is shown in Figure 10. First, time-integration simulations are performed in SIMPACK to extract the wheel-rail contact parameters. Then, the wheel wear distribution is calculated in MATLAB with non-Hertzian correction. Finally, the updated wheel profile is re-imported into SIMPACK to start the next iteration of the simulation.

Several points regarding the full-life-cycle wheel wear simulation should be clarified.

- The total simulated mileage is 200,000 km, and the wheel profile is updated every 5,000 km. Within each update interval, the actual time-integration simulation is carried out over 10 km. Therefore, the wear results obtained in each interval are scaled up by a factor of 500.
- In the track conditions, straight sections account for 80% of the route, and the curve radius ranges from 800 to 20,000 m.
- The wear values of the left and right wheels are averaged, and the wear values of the wheelsets located at longitudinally symmetric positions are also averaged.
- The wheel wear results are presented and analysed using the most severely worn wheelset.
- During the time-domain integration, wheel-rail contact forces are calculated using Hertzian contact theory and the FASTSIM algorithm. In the wear calculation stage, a non-Hertzian contact model is employed to obtain the normal force distribution within the contact patch, based on which the material removal is redistributed.

After the wheel-rail contact state variables are exported from SIMPACK, the local normal compression $c(y)$ in the wheel-rail contact region is obtained. Based on the semi-analytical strip method, the longitudinal half-length of each transverse strip is given by:

$$a(y) = \sqrt{2R_0\, c(y)} \tag{20}$$

where R_0 is the nominal rolling radius. The total normal force carried by each strip is then approximated by

$$F_{\text{strip}}(y) = \frac{\pi}{4} E^*\, c(y) \sqrt{2R_0\, c(y)} \tag{21}$$

where $E^*$is the equivalent elastic modulus. Accordingly, the weighting factor used for wear redistribution is defined

$$\omega(y) = \frac{F_{\text{strip}}(y)}{\int F_{\text{strip}}(y)\, \mathrm{d}y} \tag{22}$$

The total material removal predicted by the original Hertzian-FASTSIM-based wear calculation is then redistributed among the strips according to $\omega(y)$, while keeping the total wear amount unchanged. This correction method achieves a good balance between computational accuracy and efficiency. A more accurate conformal contact model can be found in another study by our research group [32].

The evaluation indices used in this chapter include wear-related, wheel-rail matching, and dynamic-performance indices. Specifically, wear performance is evaluated by the wheel wear depth, the wheel-rail matching state is characterised by equivalent conicity, and the dynamic performance is assessed using the wheelset lateral force F_{EN}, the bogie-frame lateral acceleration A_{EN}, and the Sperling lateral ride comfort index $W_y$listed in Table 2.

4.2. Analysis of wear evolution and wheel-rail matching states

To compare the wheel wear evolution of different schemes over the full life cycle, Figure 11 presents the wheel tread profiles after 200,000 km of service mileage, the corresponding wear distributions, and the variation in maximum wear depth with mileage for the four schemes. The comparison shows clear differences in tread wear evolution among the schemes. Among them, Ref.Fixed exhibits the most severe wear, whereas the staged configuration strategy and the further optimisation of suspension parameters both suppress wear to different extents.

As shown in Figure 11(a), after 200,000 km, the tread profiles of all four schemes evolve markedly, mainly in the working region. Ref.Staged mitigates the evolution compared with Ref.Fixed, while Opt1 and Opt2 provide further improvement. Figure 11(b) shows similar peak wear positions among the schemes, suggesting that their main effect is to reduce wear magnitude rather than change wear location. Opt2 gives the smallest wear peak. As shown in Figure 11(c), the maximum wear depth increases with mileage, with the overall level decreasing from Ref.Fixed to Ref.Staged, Opt1, and Opt2. Thus, the staged configuration slows wear accumulation, and optimised suspension parameters further enhance wear control. The resulting changes in wheel–rail matching are therefore examined through equivalent conicity.

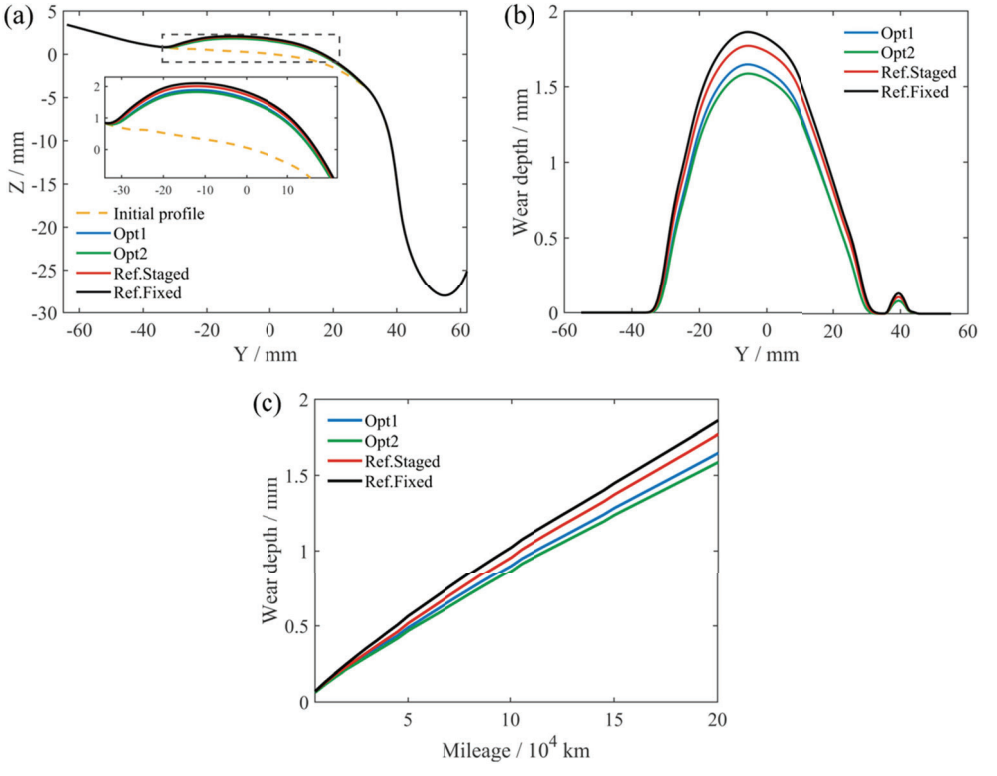


Figure 11. Comparison of tread wear under different schemes: (a) tread profiles at 200,000 km; (b) wear distribution at 200,000 km; (c) evolution of maximum wear depth.

Figure 12 presents the equivalent conicity curves at 50,000, 100,000, 150,000, and 200,000 km. The scheme differences are minor in the early stage but become clear with increasing mileage, especially at 200,000 km. Opt1 and Opt2 show more gradual conicity evolution, whereas Ref.Fixed exhibits a stronger upward shift in the later stage. This indicates that the staged configuration and parameter optimisation can reduce wear accumulation and delay the deterioration of wheel–rail matching.

Figure 13 shows the variation in nominal equivalent conicity with mileage. In the early stage, all schemes remain low and close to each other. With increasing mileage, the curves gradually diverge. Opt2 shows the slowest increase, followed by Opt1 and Ref.Staged, while Ref.Fixed rises most rapidly and reaches the highest final value. This indicates that the staged configuration and suspension-parameter optimisation can delay the increase in nominal equivalent conicity and slow the deterioration of wheel–rail matching.

Using 0.1 as the switching threshold, Ref.Fixed and Opt1 exceed this value after 135,000 km, while Opt2 and Ref.Staged exceed it after 145,000 km. Therefore, Opt1 switches to two yaw dampers on each side from 140,000 km, whereas Opt2 and Ref.Staged switch from 150,000 km. Ref.Fixed enters the high-conicity range earlier but remains unchanged due to its fixed configuration. This shows that different suspension schemes influence both wear evolution and subsequent dynamic performance through changes in wheel–rail contact geometry.

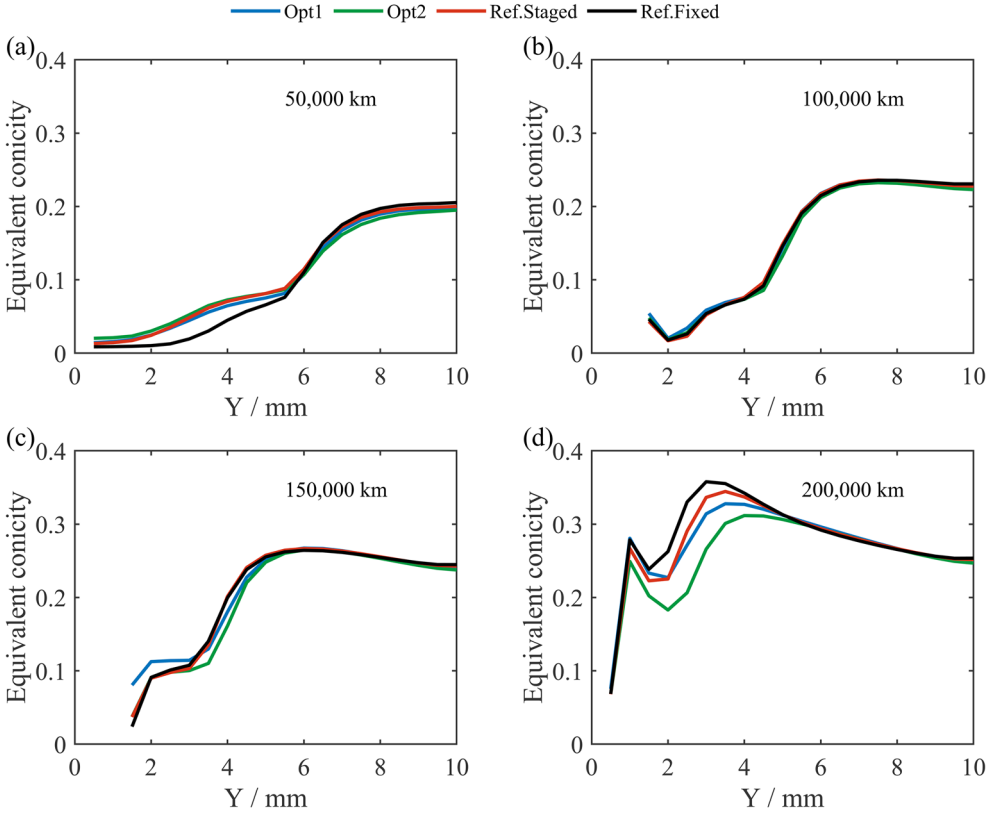


Figure 12. Comparison of equivalent conicity curves under different schemes at representative mileage nodes.

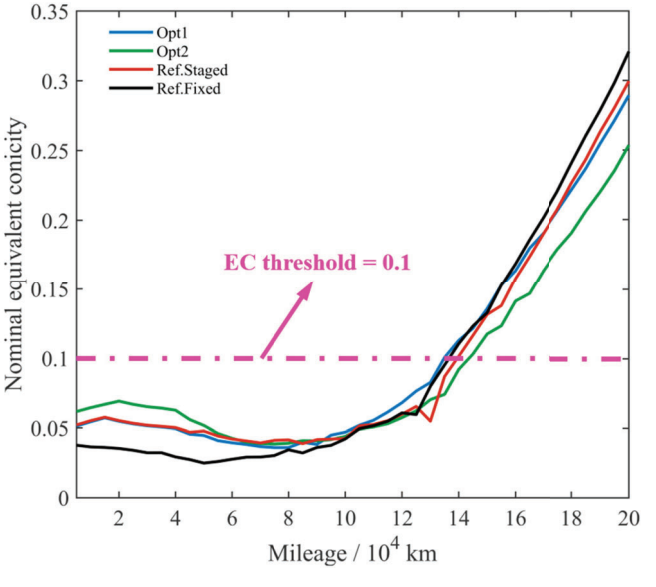


Figure 13. Variation in nominal equivalent conicity with mileage under different schemes.

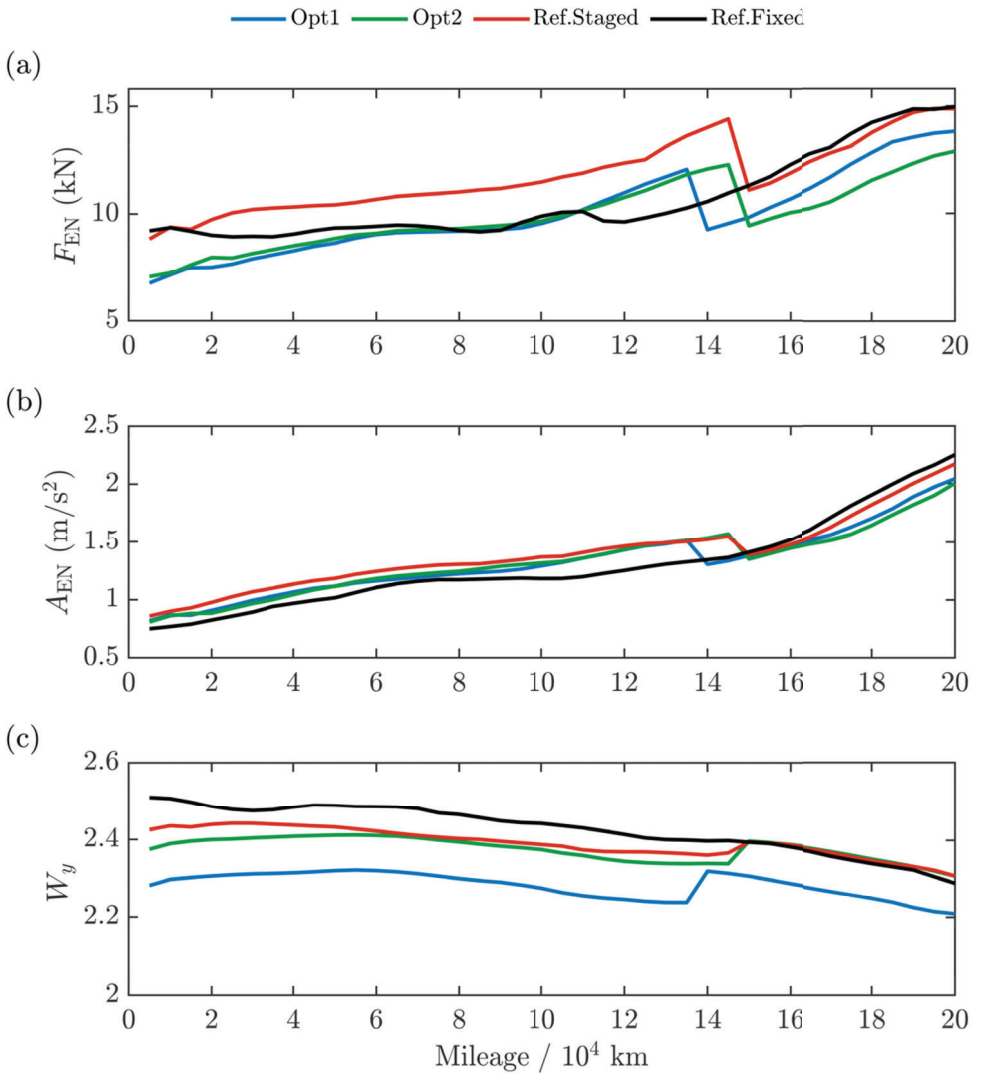


Figure 14. Evolution of dynamic performance indices with mileage under different schemes.

4.3. Dynamic performance evolution

To further evaluate the evolution of dynamic performance under different schemes over the full life cycle, Figure 14 presents the variations of F_{EN}, A_{EN}, and W_y with mileage for the four schemes. Overall, as the mileage increases, the wheel-rail matching state continues to evolve, and the lateral dynamic responses of the vehicle gradually become stronger. Meanwhile, near the staged yaw damper switching nodes, all dynamic performance indices exhibit certain stage-wise adjustment characteristics.

As shown in Figures 14(a and b), F_{EN} and A_{EN} exhibit similar trends, increasing gradually with mileage. Before damper switching, the staged schemes produce slightly higher values than Ref.Fixed, but they remain far below the later-stage levels and the limits associated with stability deterioration. After the switching criterion is reached, both responses

drop noticeably from 140,000 km for Opt1 and from 150,000 km for Opt2 and Ref.Staged, indicating that the staged configuration effectively suppresses lateral dynamic responses in the later service stage.

As shown in Figure 14(c), W_y varies more mildly, although differences among the schemes remain clear. Opt1 maintains the lowest $W_y$over the service life, followed by Opt2 and Ref.Staged, whereas Ref.Fixed remains higher. Despite slight fluctuations near the switching nodes, the optimised schemes show better ride-comfort evolution over the full life cycle.

Overall, the staged configuration emphasises later-stage robustness rather than instantaneous optimality at each mileage node. Together with the wear and conicity results, it balances wear control and dynamic-performance retention over the full life cycle. Opt1 performs slightly better in ride comfort, but Opt2 provides the best overall balance in wheel-rail force, stability, ride comfort, and wear control, and is therefore recommended for practical implementation.

5. Conclusions

This study investigated the hunting stability degradation induced by wheel wear during high-speed locomotive service. By establishing a linear dynamic model and a full-life-cycle wear simulation framework, the coupling mechanisms among suspension parameters, wheel-rail contact geometry, and hunting stability were systematically analysed. Furthermore, a supervisory staged yaw damper configuration method was proposed to adapt suspension configuration to wheel-rail contact geometry evolution. The main conclusions are summarised as follows:

(1) The low-equivalent-conicity state and high-equivalent-conicity state trigger primary and secondary hunting instabilities, respectively. Because the suspension requirements for mitigating these two modes fundamentally conflict, conventional fixed parameters cannot simultaneously satisfy the stability demands across the entire service life. This conflict is the main mechanism limiting the adaptability of fixed-parameter suspension systems during long-term operation.

(2) Root locus analysis identified the primary longitudinal stiffness, yaw damper damping, secondary lateral damper damping, yaw damper stiffness, secondary vertical stiffness, and secondary longitudinal stiffness as the key parameters affecting hunting stability under different equivalent-conicity conditions. Within the parameter ranges considered, reducing the primary longitudinal stiffness improves wear-related performance, whereas reducing the secondary lateral damper damping improves ride comfort. These results clarify the suspension-parameter sensitivity associated with different instability modes and provide the basis for stability-oriented parameter matching.

(3) The staged yaw damper configuration strategy based on nominal equivalent conicity thresholds can effectively adapt to the evolution of the wheel-rail matching state. Switching from one yaw damper per side to two at discrete mileage nodes suppresses the growth of lateral dynamic responses in the later service stage. The threshold-reaching mileage differs among schemes, indicating that suspension

design significantly affects the evolution rate of wheel-rail matching states and the hunting stability margin during service.

(4) Full-life-cycle wear simulations show that, compared with the fixed-configuration scheme, the staged configuration strategy slows wheel tread evolution and improves wear control, while further suspension-parameter optimisation enhances this effect. Among the investigated schemes, Opt2 provides the best wear suppression and equivalent-conicity control while maintaining favourable dynamic performance. Therefore, Opt2 is recommended as the preferred engineering scheme for practical implementation. This scheme effectively improves wheel-rail matching-state preservation, reduces wheelset lateral forces, and enhances hunting stability, ride quality, and wear-related performance over the full life cycle.

Overall, combining the staged yaw damper configuration strategy with suspension-parameter optimisation provides a practical way to balance wheel wear control, preservation of wheel-rail matching states, and maintenance of dynamic performance. It also provides a state-dependent suspension configuration approach for maintaining robust dynamic performance under wheel-rail contact geometry evolution. Future work will focus on the engineering implementation of the equivalent-conicity observer and validation of the proposed strategy under broader operating conditions.

Acknowledgements

Hu Li: Writing – original draft, Validation, Software, Methodology, Formal analysis, Conceptualisation. Yuan Yao: Software, Supervision, Funding acquisition. Zhiyong Shi: Writing – review & editing, Funding acquisition. Enrico Meli: Supervision, Methodology, Conceptualization .

Author contributions

CRediT: **Hu Li:** Conceptualization, Formal analysis, Methodology, Validation, Writing – original draft; **Yuan Yao:** Funding acquisition, Software, Supervision; **Zhiyong Shi:** Funding acquisition, Writing – review & editing; **Enrico Meli:** Conceptualization, Methodology, Supervision

Disclosure statement

No potential conflict of interest was reported by the authors.

Funding

This work was supported by the National Natural Science Foundation of China [grant numbers 52372403; U2268211], the National Railway Group Science and Technology Program [grant number N2025J026], the CRRC Original Technology Ten-Year Cultivation Special Project [grant number 2025CYY002], Science and Technology Research and Development Plan Project of CRRC Group Co., Ltd . [grant number 2026CTA016], and the State Key Laboratory of Rail Transit Vehicle System [grant numbers RVLHW202404; 2026RVL-T04].

Data availability statement

Data will be made available on request.

ORCID

Yuan Yao http://orcid.org/0000-0003-2279-7463

References

[1] Chen XW, Shen LJ, Hu XY, et al. Suspension parameter optimal design to enhance stability and wheel wear in high-speed trains. Veh Syst Dyn. 2024;62(5):1230–1252. doi:10.1080/00423114.2023.2224905
[2] Wang ZG, Gong D. A survey on countermeasures of railway vehicle stability decrease caused by the evolution of hollow-worn wheels. J Vib Control. 2025;31(5–6):864–877. doi:10.1177/10775463241234726
[3] Qi YY, Dai HY, Song Y, et al. Research on the characteristics of wheel hollow wear and suppression measures of high-speed trains. Tribol Trans. 2023;66(4):597–609. doi:10.1080/10402004.2023.2191659
[4] Chang C, Ding X, Ling L, et al. Mechanism of high-speed train carbody shaking due to degradation of wheel-rail contact geometry. Int J Rail Transport. 2023;11(3):289–316. doi:10.1080/23248378.2022.2077850
[5] Sun JF, Chi MR, Jin XS, et al. Experimental and numerical study on carbody hunting of electric locomotive induced by low wheel-rail contact conicity. Veh Syst Dyn. 2021;59(2):203–223. doi:10.1080/00423114.2019.1674344
[6] Bosso N, Magelli M, Zampieri N. Simulation of wheel and rail profile wear: a review of numerical models. Railw Eng Sci. 2022;30(4):403–436. doi:10.1007/s40534-022-00279-w
[7] Xie YC, Chi MR, Cai WB, et al. A framework for wheel profile wear prediction of high-speed trains considering tread modification. Friction. 2025;13(10):9441060. doi:10.26599/FRICT.2025.9441060
[8] Nencioni L, Meli E, Rindi A, et al. A new efficient conformal contact model for multibody and railway applications. Multibody Syst Dyn. 2025;64(4):587–626. doi:10.1007/s11044-024-10028-y
[9] Apezetxea IS, Perez X, Alonso A. Experimental validation of a fast wheel wear prediction model. Wear. 2021;486–487:204090. doi:10.1016/j.wear.2021.204090
[10] H-Nia S, Krishna VV, Odolinski K, et al. Simulation-based evaluation of maintenance strategies from a life cycle cost perspective. Wear. 2023;532–533:205120. doi:10.1016/j.wear.2023.205120
[11] Liu SS, He QX, Fu WJ, et al. A two-step data-driven method for predicting the wear of train wheel treads using GA-BPNN and LSTM algorithms. Int J Rail Transport. 2025;13(1):85–102. doi:10.1080/23248378.2024.2324092
[12] Wang MQ, Jia SX, Chen EL, et al. Research and application of neural network for tread wear prediction and optimization. Mech Syst Signal Process. 2022;162:108070. doi:10.1016/j.ymssp.2021.108070
[13] Chen C, Zhu F, Xu ZW, et al. Knowledge-informed wheel wear prediction method for high-speed train using multisource signal data. IEEE Trans Instrum Meas. 2024;73:1–12. doi:10.1109/TIM.2024.3413151
[14] Liu BB, Bruni S. Influence of individual wheel profiles on the assessment of running dynamics of a rail vehicle by numerical simulation: a case study. Veh Syst Dyn. 2022;60(7):2393–2412. doi:10.1080/00423114.2021.1901940
[15] Gao HX, Sun JF, Chen XH, et al. A novel wheel wear indicator in regard to wheel-rail contact parameters and vehicle hunting stability. Eng Fail Anal. 2025;167:108967. doi:10.1016/j.engfailanal.2024.108967
[16] Li H, Yao Y, Shi ZY, et al. Mechanisms of wheel wear evolution and wheel-rail contact geometry variation in locomotives. Wear. 2026;601:206842. doi:10.1016/j.wear.2026.206842
[17] Kulkarni R, Qazizadeh A, Berg M, et al. Investigating the effect of the equivalent conicity function's nonlinearity on the dynamic behaviour of a rail vehicle under typical service conditions. Veh Syst Dyn. 2022;60(10):3484–3503. doi:10.1080/00423114.2021.1962537

[18] Ye YG, Vuitton J, Sun Y, et al. Railway wheel profile fine-tuning system for profile recommendation. Railw Eng Sci. 2021;29(1):74–93. doi:10.1007/s40534-021-00234-1
[19] Cui DB, Fu YD, Wu YL, et al. Optimisation of rail profile and grinding pattern in the curve section of a subway. Veh Syst Dyn. 2024;62(7):1827–1847. doi:10.1080/00423114.2023.2266531
[20] H-Nia S, Flodin J, Casanueva C, et al. Predictive maintenance in railway systems: MBS-based wheel and rail life prediction exemplified for the Swedish Iron-Ore line. Veh Syst Dyn. 2024;62(1):3–20. doi:10.1080/00423114.2022.2161920
[21] Firlik B, Staśkiewicz T, Jaśkowski W, et al. Optimisation of a tram wheel profile using a biologically inspired algorithm. Wear. 2019;430–431:12–24. doi:10.1016/j.wear.2019.04.012
[22] Ye YG, Qi YY, Shi DC, et al. Rotary-scaling fine-tuning (RSFT) method for optimizing railway wheel profiles and its application to a locomotive. Railw Eng Sci. 2020;28(2):160–183. doi:10.1007/s40534-020-00212-z
[23] Qi YY, Dai HY, Gan F, et al. Optimisation of wheel profile of variable gauge high-speed trains. Veh Syst Dyn. 2024;62(3):651–672. doi:10.1080/00423114.2023.2186250
[24] Li H, Yao Y, Chen XW. Suspension parameter optimization for high-speed train with severe tread wear. Int J Rail Transport. 2025;13(2):381–401. doi:10.1080/23248378.2024.2345683
[25] Song Y, Qi YY, Dai HY. Multi-parameter optimization based on a surrogate model for improving vehicle dynamics and reducing wheel wear in high-speed EMUs. Veh Syst Dyn. 2026;64(2):251–274. doi:10.1080/00423114.2024.2430577
[26] Li G, Wu RD, Deng XX, et al. Suspension parameters matching of high-speed locomotive based on stability/comfort Pareto optimization. Veh Syst Dyn. 2022;60(11):3848–3867. doi:10.1080/00423114.2021.1979602
[27] Zhang XX, Li H, Cheng J, et al. Adaptive stability mechanism of high-speed train employing parallel inerter yaw damper. Veh Syst Dyn. 2023;61(1):38–57. doi:10.1080/00423114.2022.2045027
[28] Stichel S, Persson R, Giossi R. Improving rail vehicle dynamic performance with active suspension. High-Speed Rail. 2023;1(1):23–30. doi:10.1016/j.hspr.2022.12.002
[29] Li H, Tan T, Stichel S, et al. Investigating hunting stability failure in a high-speed locomotive: a comparative analysis of evaluation methods for typical worn wheel treads. Eng Fail Anal. 2025;174:109482. doi:10.1016/j.engfailanal.2025.109482
[30] EN 14363:2016 + A1. Railway applications - testing and simulation for the acceptance of running characteristics of railway vehicles - running behaviour and stationary tests. Brussels: CEN; 2016.
[31] GB/T 5599-2019. Specification for dynamic performance assessment and testing verification of rolling stock. Beijing: National Railway Administration, People's Republic of China; 2019.
[32] Nencioni L, Meli E, Rindi A, et al. A new efficient conformal contact model for multibody and railway applications. Multibody Syst Dyn. 2025;64:587–626. doi:10.1007/s11044-024-10028-y